16 (2025) 100480

Contents lists available at ScienceDirect

Carbon Capture Science & Technology

journal homepage: www.elsevier.com/locate/ccst

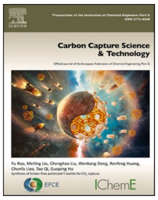

Full Length Article

Mechanisms for interactions of H_2S and Hg^0 with oxygen carrier $LaMnO_3$ during chemical looping combustion: a DFT study

Zhongze Bai [a], Kai H. Luo [a,b,*]

[a] Department of Mechanical Engineering, University College London, Torrington Place, London WC1E 7JE, UK
[b] Center for Combustion Energy, Department of Energy and Power Engineering, Key Laboratory for Thermal Science and Power Engineering of Ministry of Education, Low Carbon Energy and CCUS Research Center, Institute for Carbon Neutrality, Tsinghua University, 10084, Beijing, China

ARTICLE INFO

Keywords:
Mercury
H_2S
Density functional theory
Reaction mechanisms
Chemical looping combustion

ABSTRACT

Mercury (Hg^0) and hydrogen sulphide (H_2S) inevitably coexist during chemical looping combustion (CLC) of coal or coal-derived syngas. Their interactions with oxygen carriers are critical to understanding mercury transformation and removal. In this study, density functional theory (DFT) calculations were conducted to investigate the reaction mechanisms among Hg^0, H_2S, and the $LaMnO_3$(010) surface (a Mn-based perovskite with excellent redox properties and thermal stability). Results show that H_2S, HS, and S chemisorb on the surface via stable S-Mn bonding, while HgS forms through parallel adsorption involving both Hg-Mn and S-Mn bonds. The preferred H_2S decomposition pathway involves simultaneous dehydrogenation to produce S* and H*, with H* subsequently forming H_2 or H_2O. Among the examined reaction routes, Hg^0 reacts most favourably with S* via the Eley-Rideal mechanism, exhibiting the lowest energy barrier of 2.939 eV. These findings offer atomic-level insight into Hg-S interactions on $LaMnO_3$ surfaces and provide a theoretical foundation for the rational design of perovskite-based oxygen carriers (OCs) capable of efficient simultaneous mercury capture and sulphur stabilization, thereby advancing integrated Hg^0 and HgS removal strategies in CLC systems.

1. Introduction

Chemical looping combustion (CLC) is recognized as a promising approach for mitigating global warming, owing to its inherent capability of CO_2 separation during fossil fuel conversion (Nandy et al., 2016, Zhao et al., 2020, Bai et al., 2024). A typical CLC system comprises two reactors: a fuel reactor and an air reactor. The oxygen carrier (OC), serving as the oxygen shuttle between the two reactors, plays a pivotal role in determining system performance. Perovskite oxides, generally described by the formula ABO_3, have garnered significant attention as candidate OCs (Zhu et al., 2018). In such structures, the A-site, surrounded by twelve oxygen ions, is typically occupied by large-radius cations such as rare earth or alkaline earth metals, whereas the B-site, octahedrally coordinated by six oxygen atoms, is commonly filled by smaller transition metal cations (Ji et al., 2020). Among these, $LaMnO_3$ stands out as a Mn-based perovskite with excellent thermal stability, strong redox capability, and cost-effectiveness, making it particularly attractive for CLC applications (Ma et al., 2024, Yan et al., 2021).

Mercury (Hg), a toxic metal commonly found in coal-derived syngas, is released during combustion process predominantly in three forms: elemental mercury (Hg^0), oxidized mercury (Hg^{2+}), and particulate-bound mercury (Hg^P) (Shen et al., 2015, Yang et al., 2016). Among these, Hg^0 is typically the dominant species due to its thermodynamic stability and low aqueous solubility, which significantly hinder its effective capture (Shen et al., 2015, Yang et al., 2016). To enhance its removal, both homogeneous and heterogeneous gas–solid reactions are employed to convert Hg^0 into the more reactive Hg^{2+} or Hg^P species (Yang et al., 2017, Ji et al., 2020). The CLC process employs a wide range of OCs that not only act as oxygen transfer media but also serve as effective solid-phase catalysts for Hg^0 oxidation. Consequently, CLC presents distinct advantages over conventional combustion technologies in mitigating Hg^0 emissions. The mercury removal efficiency in such systems is largely governed by the physicochemical interactions between mercury species and the OCs.

In recent years, density functional theory (DFT) has become an indispensable tool for elucidating the reaction mechanisms of gaseous species across a broad range of chemical systems, particularly in the context of surface reactions, adsorption phenomena, and catalytic processes in heterogeneous catalysis (Bai et al., 2023, Bai et al., 2025, Bai et al., 2025). Building on this, Ma and co-workers conducted DFT

---

* Corresponding author.
E-mail address: k.luo@ucl.ac.uk (K.H. Luo).

https://doi.org/10.1016/j.ccst.2025.100480
Received 17 July 2025; Received in revised form 6 August 2025; Accepted 7 August 2025

calculations to elucidate the surface oxidation mechanism of CO on $LaMnO_3$(010) at the atomic scale (Ma et al., 2024). Their results revealed that CO preferentially adsorbs at Mn-O bridge sites, where it subsequently reacts with lattice oxygen to form a CO_2 precursor (Ma et al., 2024). This intermediate then overcomes an energy barrier of 56.03 kJ/mol to release a CO_2 (Ma et al., 2024). Similarly, Wang and co-workers employed DFT calculations to elucidate the mechanism of Hg^0 oxidation by HCl on the Mn-terminated $LaMnO_3$(010) surface, identifying a Langmuir-Hinshelwood pathway and pinpointing the formation of HgCl(ads) as the rate-determining step with an energy barrier of 0.74 eV (Wang et al., 2020). Furthermore, hydrogen sulphide (H_2S), alongside elemental mercury (Hg^0), is a toxic component in coal-derived syngas that necessitates effective removal. Notably, H_2S has been employed to modify sorbents, improving their Hg° capture efficiency on materials such as a-Fe_2O_3 (Tao et al., 2013), $CuMn_2O_4$ (Wang et al., 2020, An et al., 2023), and ceria (Ling et al., 2017). This suggests a promising route for the simultaneous removal of both pollutants. Understanding the underlying mechanisms of Hg^0 and H_2S capture is crucial for optimizing pollutant removal, enhancing the efficiency of oxygen carriers in CLC systems. However, the reaction pathways and mechanisms of H_2S interaction with Hg^0 on the $LaMnO_3$ surface have yet to be investigated.

In this study, DFT calculations were employed to elucidate the interaction mechanisms among H_2S, Hg, and $LaMnO_3$. The dissociation of H_2S proceeded through three stages ($H_2S \rightarrow HS^* + H^* \rightarrow S^* + 2H^*$) (Tao et al., 2013), and three possible surface reaction pathways were considered: Mars–van Krevelen (MvK), Eley-Rideal (E-R) and Langmuir-Hinshelwood (L-H) (Sun et al., 2015, Zhang et al., 2017). The MvK mechanism involves the reaction of gas-phase species with lattice oxygen from the solid surface; the E-R mechanism entails the direct interaction between a gas-phase molecule and an adsorbed species, while the L-H mechanism describes a surface reaction between two adsorbed species. To preliminarily identify the dominant mechanism, the adsorption behaviours of H_2S, HS, S, and HgS on $LaMnO_3$ were systematically examined, along with the energy profile of H_2S dissociation. Subsequently, all potential reaction pathways between Hg and sulphur-containing species (H_2S, HS, and S) were explored, leading to the construction of a complete reaction network. Based on energy barrier analysis, the rate-determining step was identified.

2. Methods

2.1. Computational methods

Density functional theory (DFT) simulations were conducted using the Vienna Ab Initio Simulation Package (VASP) (Kresse and Furthmüller, 1996, Kresse and Hafner, 1993), with the exchange-correlation effects described by the generalized gradient approximation (GGA) and the Perdew–Burke–Ernzerhof (PBE) functional (Perdew et al., 1996). A plane-wave basis set with an energy cutoff of 500 eV was employed. Electronic self-consistency and structural relaxations were considered converged when the total energy and residual forces reached thresholds of 1.0×10^{-5} eV and 0.03 eV/Å, respectively. Monkhorst-Pack k-point meshes of $5 \times 4 \times 5$ and $2 \times 2 \times 1$ were used for Brillouin zone sampling of the $LaMnO_3$ unit cell and supercell models, respectively. Transition states and associated energy barriers were determined via the climbing image nudged elastic band (CI-NEB) method (Henkelman et al., 2000). Supporting computational analyses were facilitated by VASPKIT (Wang et al., 2021) and QVASP (Yi et al., 2020), while visualization of structural models was performed using VESTA software (Momma and Izumi, 2008).

To facilitate the investigation of the interactions between gaseous species and OCs, the adsorption energy is evaluated as $E_{ads} = E(AB) – E(A) – E(B)$, where $E(AB)$, $E(A)$ and $E(B)$ represent the total energies of the adsorption complex, the isolated substrate and the isolated adsorbate, respectively. Besides, the energy barrier is obtained as $E_b = E(TS) – E(IS)$, and the overall reaction energy as $E_{all} = E(FS) – E(IS)$, with $E(TS)$, $E(IS)$ and $E(FS)$ denoting the energies of the transition state, initial state and final state, respectively. All adsorption energies and reaction barriers included zero-point energy (ZPE) corrections, which were calculated from vibrational frequency analyses of the optimized structures.

2.2. Models

The crystallographic structure of $LaMnO_3$, characterized by an orthorhombic lattice and classified under the Pnma space group, was sourced from the Materials Project database (MP-17554) (Jain et al., 2013). Fig. 1a illustrates the optimized configuration of the $LaMnO_3$ unit cell. Among the various low-index surfaces, the (010) facet has been identified as exhibiting superior thermodynamic stability and catalytic activity (Gavin and Watson, 2017). Comparative analyses have further demonstrated that the Mn-terminated (010) surface is more favourable than its La-terminated counterpart in terms of both stability and reactivity (Piskunov et al., 2008). Based on these findings, the Mn-terminated $LaMnO_3$(010) surface was selected for detailed investigation. A p(2×2) supercell model containing eight atomic layers was constructed, with a 20 Å vacuum region applied perpendicular to the surface to prevent interactions between periodic slabs. To balance accuracy and computational cost, the top four atomic layers were fully relaxed during geometry optimization, while the bottom four layers were fixed. Post-optimization, six distinct adsorption sites were identified on the surface, namely Mn, O_1, O_2, bridge$_1$, bridge$_2$, and hollow, as depicted in Fig. 1b.

3. Results and discussion

3.1. H_2S dissociation on $LaMnO_3$ surface

According to previous studies, H_2S undergoes dissociative adsorption on metal surfaces, producing intermediates such as HS, S, and H (Tao et al., 2013). In this section, we first investigate the dissociation process of H_2S. Fig. 2 illustrates the optimized adsorption configurations of key species involved in H_2S dissociation (H_2S, HS, S, and H) on the $LaMnO_3$(010) surface. The relevant adsorption energies and Bader charges are listed in Table 1. Two different adsorption configurations of H_2S are identified on the $LaMnO_3$ (010) surface: adsorption at the Mn site (structure 1A) and the hollow site (structure 1B), with adsorption energies of –0.693 eV and –0.144 eV, respectively. In structure 1A, H_2S transfers 0.17 *e* to the surface, indicating strong chemisorption. In contrast, structure 1B exhibits negligible charge transfer, with only 0.01 *e* transferred from the surface to H_2S. Thus, structure 1A is thermodynamically more stable than 1B. Besides, the HS intermediate exhibits a single stable adsorption configuration (1C) on the $LaMnO_3$(010) surface, where it binds at the Mn site through an S-Mn bond with a length of 2.197 Å. The adsorption energy is –2.745 eV, accompanied by a charge

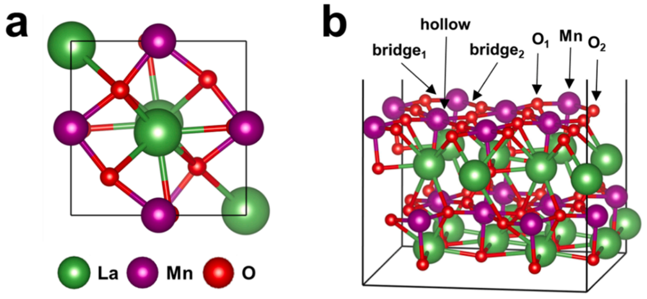

Fig. 1. Schematic illustration of the $LaMnO_3$(010) surface structures. (a) Optimized unit cell of $LaMnO_3$; (b) Mn-terminated $LaMnO_3$(010) surface model constructed as a supercell slab cleaved along the (010) direction. This figure is adapted from our previous work (Bai and Luo, 2025).

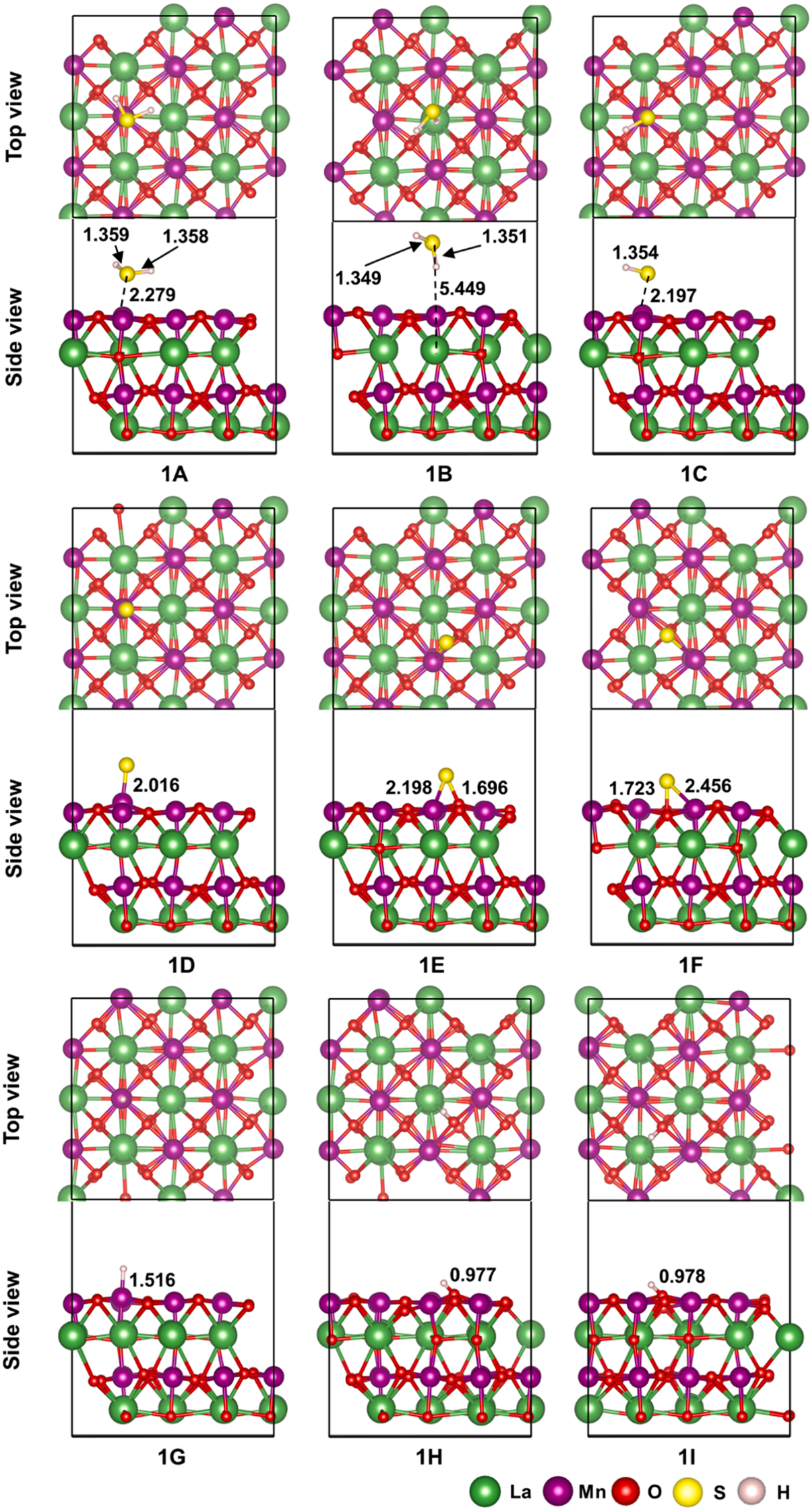

Fig. 2. Adsorption configurations of H_2S, HS, S, and H on $LaMnO_3(010)$ surface. Bond lengths are given in Angstroms (Å).

Table 1
Summary of adsorption energies (E_{ads}, eV) and Bader charge transfer (Q, e) for H_2S/HS/S adsorption on $LaMnO_3(010)$ surface (1A-1I) and HgS adsorption on $LaMnO_3(010)$ surface (2A-2J). A negative charge transfer value indicates electron transfer from the adsorbate to the surface.

ID	E_{ads}	Q	ID	E_{ads}	Q
1A	–0.693	–0.17	**2A**	–1.629	0.24
1B	–0.144	0.01	**2B**	–1.353	0.02
1C	–2.745	0.24	**2C**	–1.322	0.03
1D	–4.275	0.32	**2D**	–3.128	0.22
1E	–3.500	–0.19	**2E**	–3.241	0.23
1F	–3.280	–0.08	**2F**	–2.803	0.27
1G	–3.348	0.16	**2G**	–2.797	0.28
1H	–3.501	–0.64	**2H**	–2.731	0.34
1I	–3.407	–0.66	**2I**	–1.966	–0.16
			2J	–1.793	–0.04

transfer of 0.24 *e*. For S adsorption, three stable adsorption configurations were identified on the $LaMnO_3(010)$ surface, located at Mn, bridge$_1$, and O_2 sites (structures 1D-1F). Among them, S adsorption at the Mn site (1D) is the most stable, with an adsorption energy of –4.275 eV, forming an S-Mn bond of 2.016 Å and involving a charge transfer of 0.32 *e*. The relative stability of the configurations follows the order: 1D > 1E > 1F. Finally, H atoms preferentially adsorb at Mn, O_1, and O_2 sites on the $LaMnO_3(010)$ surface (structures 1G-1I). The most stable configuration occurs at the O_1 site (1H), where an H–O bond forms with a bond length of 0.977 Å, an adsorption energy of –3.501 eV, and a charge transfer of 0.64 *e* from H to the surface. Overall, H_2S, HS, S, and H can all form stable chemisorbed configurations on $LaMnO_3(010)$, accompanied by obvious charge transfer.

To gain further insight into the adsorption mechanisms of H_2S, HS, S, and H on the $LaMnO_3(010)$ surface, we analysed the projected density of states (PDOS) of their most stable configurations (1A, 1C, 1D, and 1H), as shown in Fig. 3. In the adsorption structures of H_2S, HS, and S, strong hybridization between the S-p and Mn-d orbitals is observed at approximately –4.5 eV, –2.5 eV, and –2.0 eV, respectively. This indicates the formation of S-Mn bond and the chemical interaction between the adsorbates and the $LaMnO_3(010)$ surface. Furthermore, the hybridization centres of H_2S, HS, and S progressively shift closer to the Fermi level as the number of hydrogen atoms decreases, which aligns with the observed trend of increasing adsorption strength on the $LaMnO_3(010)$ surface from H_2S to S. Additionally, as shown in Fig. 3d, the H-s orbital exhibits hybridization with the O-p orbital around –8 eV, indicating the formation of the H–O bond and chemical adsorption of H on the $LaMnO_3(010)$ surface.

Based on previous studies, elemental mercury (Hg^0) can react with sulphur-containing compounds on metal surfaces to form HgS (Tao et al., 2013, Wang et al., 2020, An et al., 2023, Ling et al., 2017). Therefore, investigating the reaction mechanisms of H_2S on the $LaMnO_3(010)$ surface serves as a critical first step, as shown in Fig. 4. It is important to note that in the calculation of the energy profiles

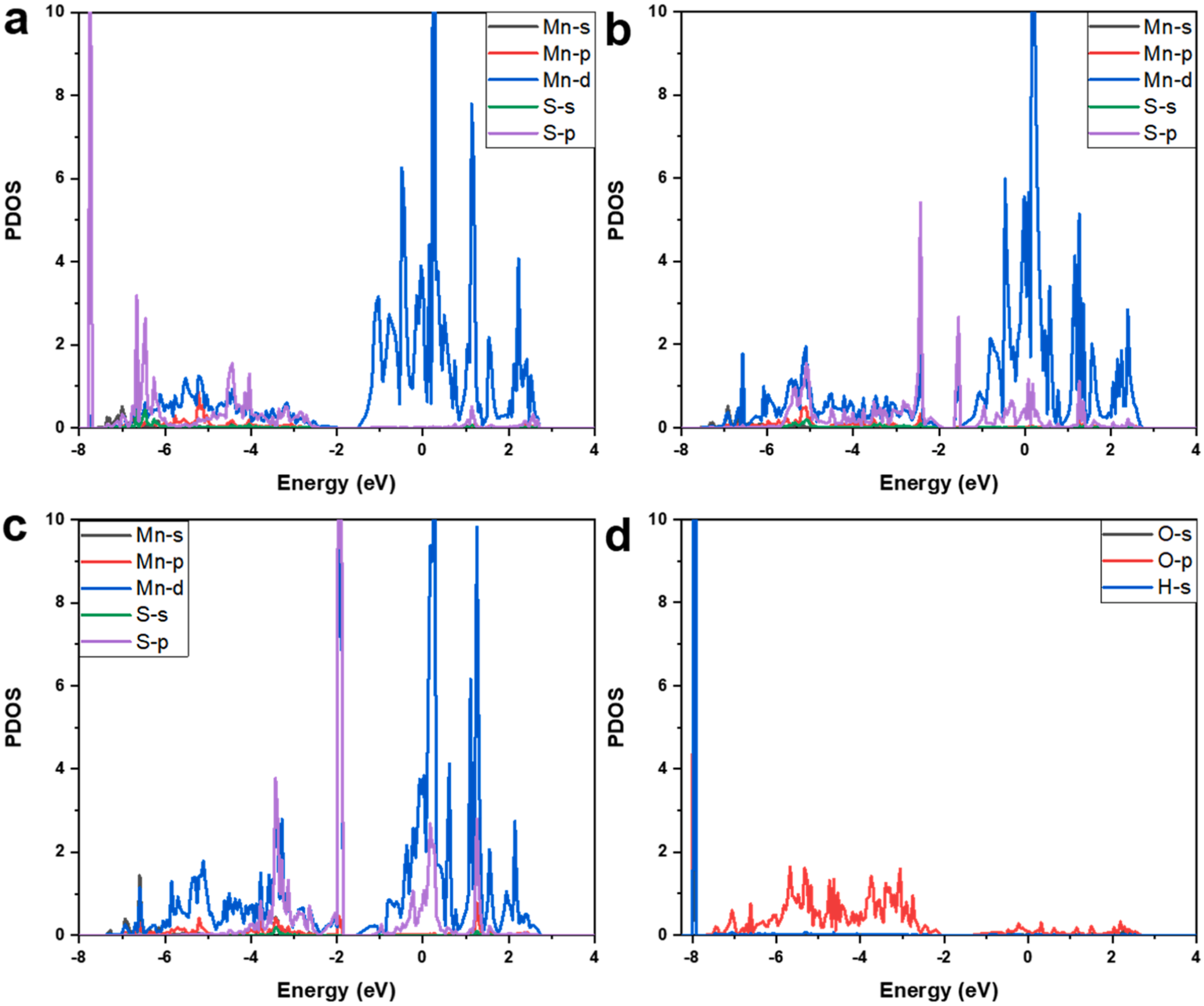

Fig. 3. PDOS for (a) S and Mn atoms in configuration 1A, (b) S and Mn atoms in configuration 1C, (c) S and Mn atoms in configuration 1D, and (d) H and O atoms in configuration 1H.

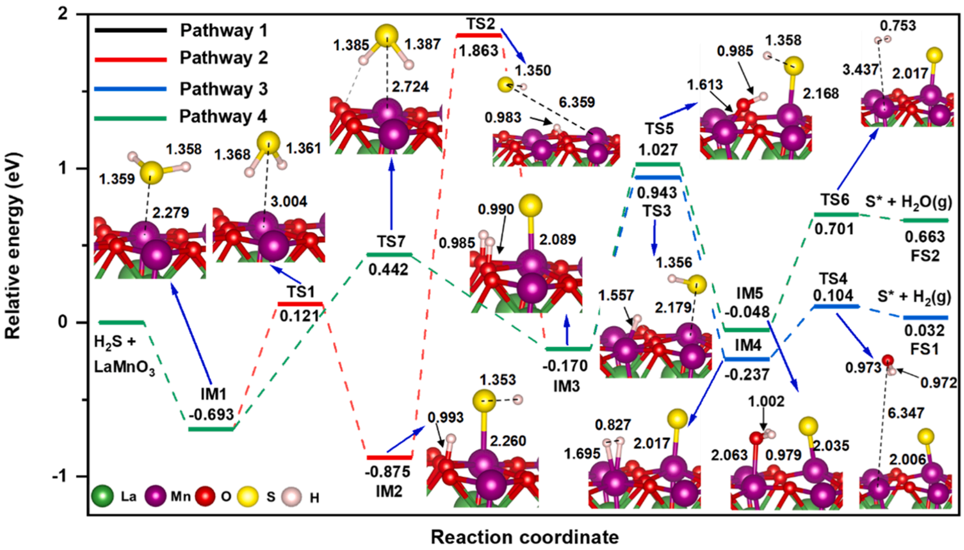

Fig. 4. The potential energy diagram for H_2S dissociation and subsequent reactions on $LaMnO_3$(010) surface. Bond lengths are given in Angstroms (Å). Note: Pathway 1 is not explicitly shown in the figure because its H_2S dissociation step is identical to that of Pathway 2, and its oxidation step overlaps with that of Pathway 3. Consequently, the steps of Pathway 1 are fully represented by the overlapping segments of Pathways 2 and 3.

presented in Figs. 4, 8–10, the most stable configuration of each intermediate is selected for analysis. Overall, the reaction of H_2S proceeds through four possible pathways and involves two key steps: the dissociation of H_2S and the subsequent formation of either H_2 or H_2O.

In the first dissociation stage, H_2S initially adsorbs onto the $LaMnO_3$(010) surface, forming an S-Mn bond with a bond length of 2.279 Å (structure IM1). Upon dehydrogenation, S* and two H* species are generated (IM3), with the S atom remaining bonded to the Mn site. The S-Mn bond shortens to 2.089 Å, while the H atoms migrate to adjacent O_1 sites, forming H–O bonds with lengths of 0.985 Å and 0.990 Å, respectively. Two dehydrogenation pathways were considered. In the first pathway, H_2S* undergoes stepwise dehydrogenation: one H atom is first removed to form HS* + H*, overcoming an energy barrier of 0.814 eV at transition state TS1; the second H atom is then removed to yield IM3, with an associated energy barrier of 2.737 eV at TS2. It is evident that the energy barrier for the first dehydrogenation step is significantly lower than that for the second, which is consistent with previous studies (An et al., 2023, Zheng and Zhao, 2021). In the alternative pathway, H_2S* simultaneously loses both hydrogen atoms to form IM3 via TS7, with a single-step energy barrier of 1.135 eV. Therefore, compared to stepwise dehydrogenation, the concerted dehydrogenation pathway is more favourable during the reaction, owing to its lower energy barrier.

In the subsequent stage involving the formation of gaseous products, the reaction pathway for H_2 formation proceeds as IM3 → TS3 → IM4 → TS4 → H_2 (g), with the rate-determining step being IM3 → TS3 → IM4 and an energy barrier of 1.113 eV. For H_2O formation, the pathway follows IM3 → TS5 → IM5 → TS6 → H_2O(g), with the rate-determining step being IM3 → TS5 → IM5 and an energy barrier of 1.197 eV.

To sum up, the most favourable reaction pathway for H_2S on the $LaMnO_3$(010) surface is pathway 4: H_2S → IM1 → TS7 → IM3 → TS3 → IM4 → TS4 → H_2(g), with the rate-determining step being IM1 → TS7 → IM3 and an associated energy barrier of 1.135 eV (Fig. 4).

3.2. Interaction of HgS on $LaMnO_3$ surface

Since Hg serves as the reactant and HgS as the product in the overall reaction, investigating their adsorption behaviours on the $LaMnO_3$(010) surface is crucial for elucidating the reaction mechanisms. Given that the adsorption of Hg has already been thoroughly examined in our previous work (Bai and Luo, 2025), the present study focuses on the adsorption behaviour of HgS on the $LaMnO_3$(010) surface. By examining all possible adsorption sites and orientation, including both perpendicular (Hg-down and S-down) and parallel configurations, ten energetically stable structures are identified, as shown in Fig. 5.

In the perpendicular (Hg-down) adsorption situations, three stable configurations (2A–2C) are identified, corresponding to adsorption at Mn, O_1, and O_2 sites. Among them, Hg adsorption at the Mn site (2A) is the most stable, featuring an adsorption energy of –1.629 eV and an Hg-Mn bond length of 2.521 Å. Under parallel adsorption configurations, the S atom preferentially binds to the Mn atom. In structures 2D and 2E, the Hg atom is also adsorbed on a Mn atom, with an O atom situated between two adjacent Mn atoms. For clarity in describing the structural configurations, these configurations are classified as A-C-B types, where atom C is located between two adsorption sites, A and B. Accordingly, the two structures are designated as Mn-O_1-Mn and Mn-O_2-Mn adsorption configurations, respectively. In contrast, in structures 2F and 2G, the Hg atom is located at hollow sites. Among all configurations, structure 2E is the most stable, exhibiting an adsorption energy of –3.241 eV and a charge transfer of 0.23 *e*, indicating a strong chemisorption. For the perpendicular (S-down) adsorption mode, three types of adsorption sites (Mn, $Bridge_1$, and O_2) are found (2H–2J). In those cases, the Hg-S bond dissociates upon adsorption, preventing stable binding of HgS on the $LaMnO_3$(010) surface. Overall, the parallel adsorption mode results in more stable interactions, with the Mn-O_2-Mn configuration being the most energetically favourable.

Furthermore, the PDOS analysis of the most stable HgS adsorption configuration (2E) was carried out to elucidate the adsorption mechanisms between HgS and the $LaMnO_3$(010) surface, as shown in Fig. 6. It is obvious that the Hg-s orbital exhibit strong hybridization with the neighbouring Mn-d-orbital at approximately –1.4 eV, while the S-p orbitals strongly hybridize with adjacent Mn-d orbitals near –1.7 eV. Additionally, a pronounced hybridization between the Hg-s and S-p orbitals is observed around –1.4 eV. These features indicate that HgS undergoes chemical adsorption on the $LaMnO_3$ surface, leading to the formation of Hg-Mn and S-Mn bonds. Meanwhile, the Hg-S bond remains intact throughout the adsorption process.

3.3. Reaction Mechanisms of Hg with sulphur-containing species on the $LaMnO_3$ surface

To further elucidate the reaction mechanisms of Hg^0 and sulphur-containing species on the $LaMnO_3$ surface, all possible interaction

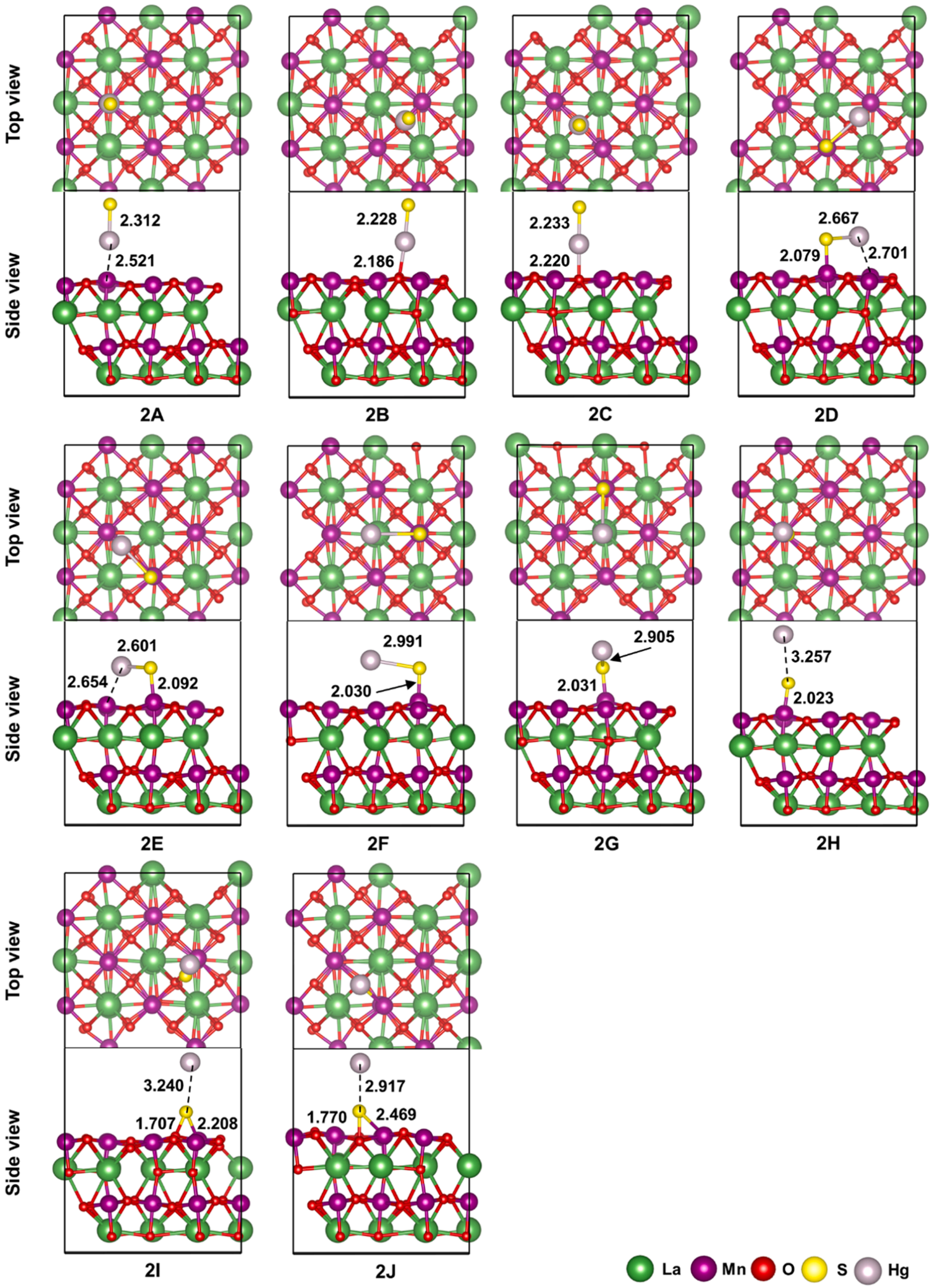

Fig. 5. Adsorption configurations of HgS on $LaMnO_3(010)$ surface. Bond lengths are given in Angstroms (Å).

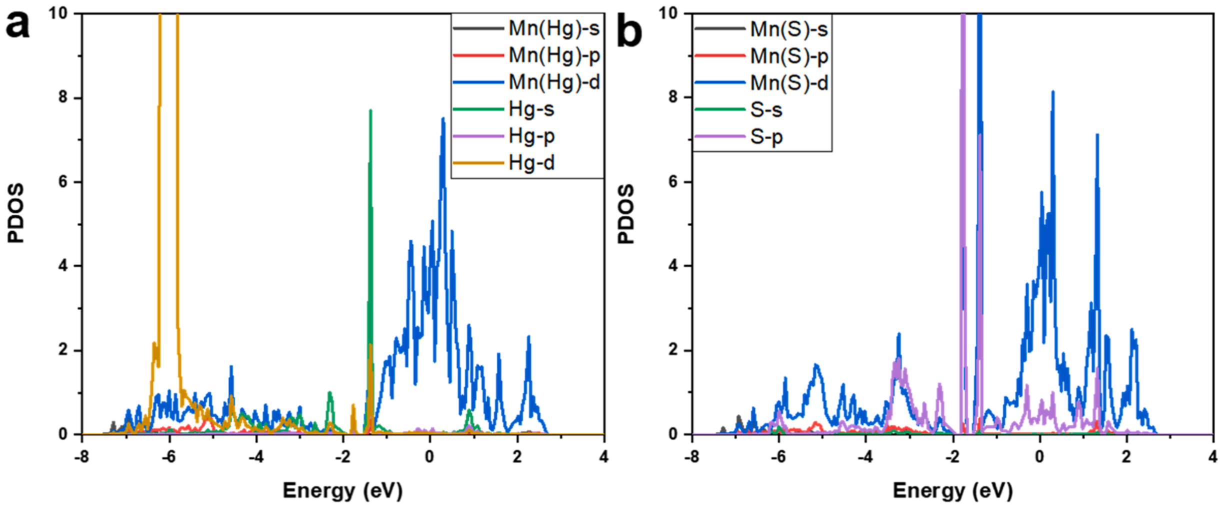

Fig. 6. PDOS for (a) Mn and Hg atoms and (b) S and Mn atoms in configuration 2E.

pathways are considered, including both E-R and L-H mechanisms. The configurations presented in Fig. 7 depict Hg^0 adsorbed onto $LaMnO_3$ surfaces pre-covered with H_2S, HS, or S species. In all adsorption configurations, the Hg^0 atom is positioned directly above the sulphur atom. According to the E-R mechanism, H_2S, HS, or S is pre-adsorbed on the $LaMnO_3$ surface, and the corresponding reaction pathways are as follows:

$$H_2S^* + Hg^0(g) \rightarrow HgS(g) + 2H^*$$

$$HS^* + Hg^0(g) \rightarrow HgS(g) + H^*$$

$$S^* + Hg^0(g) \rightarrow HgS(g)$$

The geometries shown in Fig. 7a–c are considered the initial states of these E-R reactions, respectively. In line with the L-H mechanism, the following surface reactions are also examined:

$$H_2S^* + Hg^* \rightarrow HgS^* + 2H^*$$

$$HS^* + Hg^* \rightarrow HgS^* + H^*$$

$$S^* + Hg^* \rightarrow HgS^*$$

The configurations shown in IM9 (Fig. 8), IM11 (Fig. 9), and IM13 (Fig. 10) are considered the initial states of the respective L-H reactions. The detailed reaction mechanisms are discussed below:

3.3.1. *Hg^0 reacts with H_2S^**

The potential energy diagram for the pathways between H_2S^* and either gaseous or adsorbed Hg^0 is presented in Fig. 8. Under the E-R mechanism, Hg^0 directly reacts with pre-adsorbed H_2S to form gaseous HgS, with an energy barrier of 3.877 eV at the transition state TS8. During this process, the S and Hg atoms gradually approach each other to form an Hg-S bond while moving away from the $LaMnO_3(010)$ surface, and the hydrogen atoms dissociate from S and adsorb onto the surface. The overall reaction is endothermic, with a reaction energy of 3.176 eV.

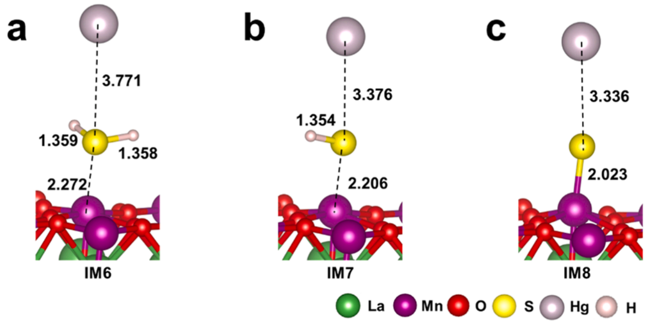

Fig. 7. Optimized configurations of Hg^0 adsorption on $LaMnO_3(010)$ surfaces pre-adsorbed with (a) H_2S, (b) HS, and (c) S species. Bond lengths are given in Angstroms (Å).

In the L-H mechanism, Hg^0 first adsorbs onto the $LaMnO_3(010)$ surface pre-covered with H_2S, forming intermediate IM9. The adsorption site corresponds to the Mn atom within a Mn-O_2-Mn configuration, which has previously been identified as the most stable configuration for HgS adsorption. Subsequently, the system proceeds through the formation and desorption of surface-bound HgS via the pathway IM9 → TS9 → IM10 → TS10 → HgS(g). The rate-determining step is IM10 → TS10 → HgS(g), requiring an energy barrier of 3.207 eV. The overall reaction is also endothermic, with a reaction energy of 3.030 eV.

In summary, since the L-H mechanism involves a lower energy barrier (3.207 eV) compared to the E-R mechanism (3.877 eV), the formation of HgS is more likely to proceed via the L-H pathway.

3.3.2. *Hg^0 reacts with HS**

As shown in Fig. 9, the potential energy profiles of two reaction pathways between HS* and either gaseous or adsorbed Hg^0 were calculated. The results indicate that HgS can be formed via the E-R mechanism ($HS^* + Hg(g) \rightarrow HgS(g) + H^*$), with an energy barrier of 3.509 eV, during which the hydrogen atom transfers to a neighbouring oxygen atom on the $LaMnO_3(010)$ surface.

For the L-H pathway, Hg^0 first adsorbs onto the $LaMnO_3(010)$ surface pre-covered with HS*, forming the intermediate IM11. The adsorption site is identical to that in IM9 from Fig. 8. Subsequently, the distance between Hg and S decreases, leading to the formation of an Hg-S bond and eventual desorption of HgS along the pathway IM11 → TS12 → IM12 → TS13 → HgS(g). The rate-determining step of this pathway is the desorption of HgS (IM12 → TS13 → HgS(g)), with E_b of 3.254 eV.

Both the E-R and L-H mechanisms are endothermic, with reaction energies of 3.105 eV, respectively. However, due to its lower energy barrier, the L-H pathway is thermodynamically and kinetically more favourable.

3.3.3. *Hg^0 reacts with S**

The potential energy diagram for the two reaction pathways between adsorbed S* and gaseous or adsorbed Hg^0 is presented in Fig. 10. Overall, regardless of whether the reaction proceeds via the E-R or L-H mechanism, the entire process is endothermic with a reaction energy of 2.688 eV.

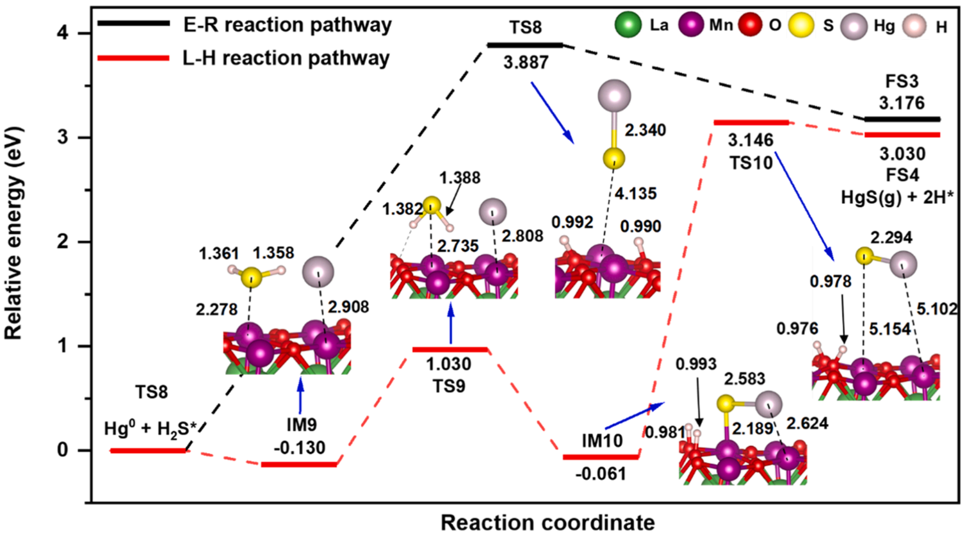

Fig. 8. Energy profile and optimized geometries for the reaction between H_2S^* and Hg^0 on the $LaMnO_3(010)$ surface (symbol * denotes an adsorbed intermediate species). Bond lengths are given in Angstroms (Å).

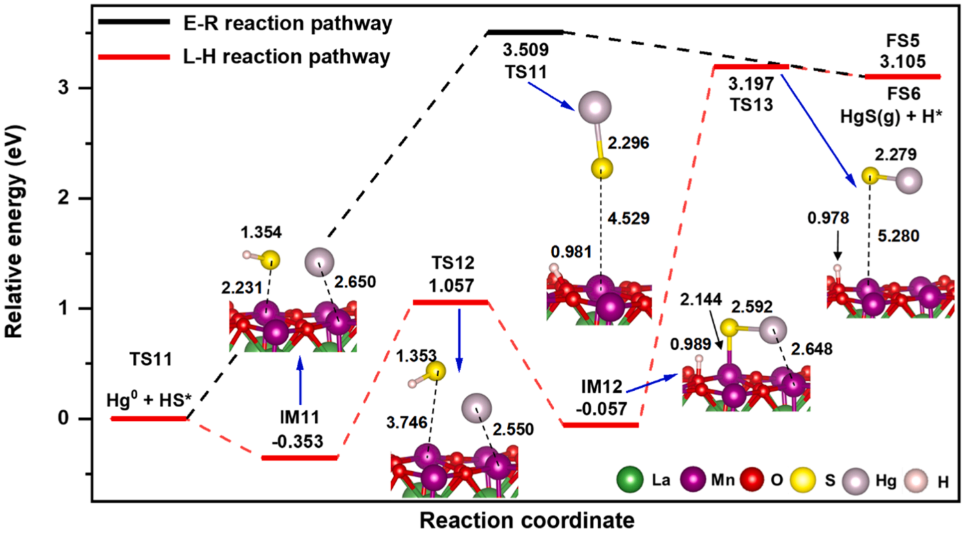

Fig. 9. Energy profile and optimized geometries for the reaction between HS^* and Hg^0 on the $LaMnO_3(010)$ surface (symbol * denotes an adsorbed intermediate species). Bond lengths are given in Angstroms (Å).

For the E-R mechanism, the direct reaction between S* and gaseous Hg^0 ($S^* + Hg(g) \rightarrow HgS(g)$) proceeds with an energy barrier of 2.939 eV. In contrast, under the L-H mechanism, Hg^0 first adsorbs onto an Mn site on the $LaMnO_3$ surface, forming intermediate IM13. Notably, this adsorption site differs from those in IM9 (Fig. 8) and IM11 (Fig. 9), as it is located farther from the pre-adsorbed S atom. Subsequently, the Hg atom migrates toward the S atom to form an adsorbed HgS species via the pathway IM13 → TS15 → IM14. The final step involves the desorption of HgS through the transition state TS16, completing the pathway IM14 → TS16 → HgS(g). The rate-determining step of the L-H mechanism exhibits an energy barrier of 3.436 eV at TS16.

Unlike the reactions involving H_2S and HS, the E-R pathway exhibits a lower energy barrier in the case of S*, indicating that the formation of HgS is more favourable via the E-R mechanism.

3.4. Discussion

Based on the above mechanistic analysis of Hg^0 reacting with H_2S, HS, and S, it can be concluded that as H_2S undergoes progressive dissociation, the energy barrier of the E-R mechanism gradually decreases, while that of the L-H mechanism increases. This trend ultimately leads to a mechanistic shift from L-H to E-R in the reaction between Hg^0 and S. Among all pathways, the reaction of Hg^0 with S via the E-R mechanism exhibits the lowest energy barrier of 2.939 eV.

Considering both the energy profiles of H_2S dissociation and subsequent HgS formation, the overall most favourable reaction pathway involves the direct dehydrogenation of H_2S to form adsorbed S, which then reacts with gaseous Hg^0 via the E-R mechanism to yield HgS that subsequently desorbs. The hydrogen atoms are ultimately released as either H_2 or H_2O. The rate-determining step along this optimal pathway features an energy barrier of 2.939 eV. According to our previous study (Bai and Luo, 2025), the energy barriers for HgO formation via reaction with lattice oxygen atoms O_1 and O_2 are 4.403 eV and 4.538 eV, respectively, while the barrier via reaction with adsorbed O_2 is significantly lower at 1.354 eV. These results indicate that HgS formation is more favourable than HgO formation involving lattice oxygen, but less favourable compared to the pathway involving adsorbed O_2.

The relatively high energy barrier of 2.939 eV for HgS formation

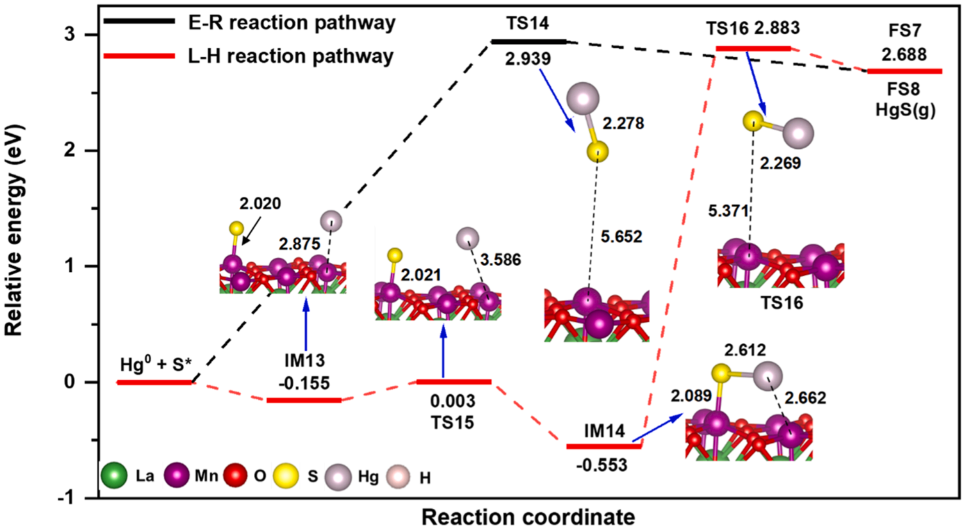

Fig. 10. Energy profile and optimized geometries for the reaction between S* and Hg^0 on the $LaMnO_3(010)$ surface (symbol * denotes an adsorbed intermediate species). Bond lengths are given in Angstroms (Å).

suggests that this step is kinetically demanding. Fortunately, the high operating temperatures of chemical looping combustion (CLC) systems, typically between 800 and 1000 °C, provide favourable conditions to overcome this kinetic barrier and facilitate effective HgS formation in practical combustion environments. Although this barrier may pose a challenge for efficient mercury capture, the HgS formation pathway remains the most kinetically favourable among those studied, offering mechanistic insight into Hg° transformation in reactive flue gas. This limitation may be addressed through appropriate temperature control and the development of more active OCs. While reaction rates were not calculated in this study, evaluating the practical feasibility of HgS formation is an important direction for future research. Predicting macroscopic reaction rates from first-principle data will require multi-scale modelling from atomic-level surface reactions to reactor-scale kinetics, to be developed and validated with experimental data in subsequent work.

It is worth noting that although the PBE functional was adopted in this study, it has known limitations in describing strongly correlated electron systems such as $LaMnO_3$, particularly in underestimating band gaps and delocalizing Mn-d electrons. Nevertheless, previous studies on $LaMnO_3$-based materials in CLC systems have demonstrated that the PBE functional can reliably reproduce key calculated data such as reaction energies and activation barriers, showing good agreement with experimental observations (Ma et al., 2024, Wang et al., 2020). Based on this precedent and to ensure consistency with existing literature, the standard PBE functional was employed in the present work. In future studies, more advanced approaches such as DFT+U or hybrid functionals could be utilized to better capture the localized d-electron behaviour and further improve the quantitative accuracy of surface reaction energetics and electronic structure predictions. Where possible, these computational improvements should also be complemented by experimental validation to ensure the reliability and applicability of theoretical results in practical systems.

4. Conclusions

In this study, DFT calculations were performed to explore the surface reaction mechanisms of H_2S and Hg^0 on the $LaMnO_3(010)$ surface. The key findings are summarized as follows:

1) H_2S and its decomposition products (HS*, S*) exhibit strong chemisorption on $LaMnO_3(010)$, forming stable S–Mn bonds. HgS also chemisorbs stably through both Hg–Mn and S–Mn coordination in a parallel configuration.
2) The most favourable H_2S decomposition pathway involves simultaneous dehydrogenation, forming surface-bound S* and H*, followed by the desorption of H_2 or H_2O.
3) Among the evaluated routes, the formation of HgS via the E–R mechanism between gas-phase Hg^0 and surface S* exhibits the lowest energy barrier (2.939 eV), indicating it is the most kinetically favourable pathway.

These results provide atomic-level insights into the coupled transformation of sulphur- and mercury-containing species on $LaMnO_3$. Stabilizing them into HgS is advantageous, as HgS is a thermally stable, low-volatility solid that is more readily captured than gaseous SO_2 and less prone to re-emission than HgO, making it a more manageable form for pollutants control. Importantly, this study highlights the potential of $LaMnO_3$-based oxygen carriers to simultaneously capture Hg^0 and convert sulphur species into HgS during CLC, offering a dual-function strategy that integrates adsorption and catalytic transformation within a single material. Furthermore, the high barrier for HgS formation highlights the need to lower rate-limiting steps, e.g., via B-site doping or oxygen vacancy engineering, to improve catalytic efficiency. This work provides a theoretical foundation for designing multifunctional perovskite oxygen carriers for clean coal technologies.

CRediT authorship contribution statement

Zhongze Bai: Writing – original draft, Visualization, Validation, Software, Methodology, Investigation, Formal analysis, Data curation, Conceptualization. **Kai H. Luo:** Writing – review & editing, Supervision, Resources, Project administration, Funding acquisition.

Declaration of competing interest

The authors declare that they have no known competing financial interests or personal relationships that could have appeared to influence the work reported in this paper.

Acknowledgements

The research is supported by Carbon Neutrality and Energy System Transformation (CNEST) Program led by Tsinghua University. Support from the UK Engineering and Physical Sciences Research Council under the project “UK Consortium on Mesoscale Engineering Sciences (UKCOMES)” (Grant No. EP/X035875/1) is also acknowledged. This work made use of computational support by CoSeC, the Computational Science Centre for Research Communities, through UKCOMES.

References

An, M., Guo, Q., Wei, X., 2023. Reaction mechanism of H2S with Hg0 on CuFe2O4 oxygen carrier with oxygen vacancy structure during coal chemical looping gasification. Fuel 333, 126477.

Bai, Z., Jiang, X.Z., Luo, K.H., 2023. Theoretical exploration on the performance of single and dual-atom Cu catalysts on the CO 2 electroreduction process: a DFT study. Phys. Chem. Chem. Phys. 25 (35), 23717–23727.

Bai, Z., Jiang, X.Z., Luo, K.H., 2024. Effects of Electric Field on Chemical Looping Combustion: A DFT Study of CO Oxidation on CuO (111) Surface. ACS Omega 9 (19), 21082–21088.

Bai, Z., Jiang, X.Z., Luo, K.H., 2025. Enhanced CO2 electrochemical reduction on single-atom catalysts with optimized environmental, central and axial chemical ambient. J. Colloid. Interface Sci.

Bai, Z., Luo, K.H., 2025. Mechanistic study of Hg0 oxidation over LaMnO3 oxygen carrier during chemical looping combustion. Chem. Eng. J., 166154

Bai, Z., Zhi, Z., Jiang, X.Z., Luo, K.H., 2025. Rational Design of Dual-Atom Catalysts for Electrochemical CO2 Reduction to C1 and C2 Products with High Activity and Selectivity: A Density Functional Theory Study. Ind. Eng. Chem. Res. 64 (8), 4378–4387.

Gavin, A.L., Watson, G.W., 2017. Modelling oxygen defects in orthorhombic LaMnO 3 and its low index surfaces. Phys. Chem. Chem. Phys. 19 (36), 24636–24646.

Henkelman, G., Uberuaga, B.P., Jónsson, H., 2000. A climbing image nudged elastic band method for finding saddle points and minimum energy paths. J. Chem. Phys. 113 (22), 9901–9904.

Jain, A., Ong, S.P., Hautier, G., Chen, W., Richards, W.D., Dacek, S., et al., 2013. Commentary: the materials project: a materials genome approach to accelerating materials innovation. APL Mater. 1 (1).

Ji, L., Wang, Q., Zhang, Z., Wu, H., Zhou, C., Yang, H., 2020. Release characteristics of mercury in chemical looping combustion of bituminous coal. J. Environ. Sci. 94, 197–203.

Ji, Q., Bi, L., Zhang, J., Cao, H., Zhao, X.S., 2020. The role of oxygen vacancies of ABO 3 perovskite oxides in the oxygen reduction reaction. Energy Environ. Sci. 13 (5), 1408–1428.

Kresse, G., Furthmüller, J., 1996. Efficiency of ab-initio total energy calculations for metals and semiconductors using a plane-wave basis set. Comput. Mater. Sci. 6 (1), 15–50.

Kresse, G., Hafner, J., 1993. Ab initio molecular dynamics for liquid metals. Phys. Rev. B 47 (1), 558.

Ling, L., Zhao, Z., Zhao, S., Wang, Q., Wang, B., Zhang, R., et al., 2017. Effects of metals doping on the removal of Hg and H2S over ceria. Appl. Surf. Sci. 403, 500–508.

Ma, X., Liu, J., Yang, Y., 2024. Experimental and theoretical studies on the reactivity and reaction mechanism of LaMnO3 with CO in chemical looping combustion. J. Energy Instit. 112, 101462.

Momma, K., Izumi, F., 2008. VESTA: a three-dimensional visualization system for electronic and structural analysis. Appl. Crystallogr. 41 (3), 653–658.

Nandy, A., Loha, C., Gu, S., Sarkar, P., Karmakar, M.K., 2016. Chatterjee PK. Present status and overview of chemical looping combustion technology. Renew. Sustain. Energy Rev. 59, 597–619.

Perdew, J.P., Burke, K., Ernzerhof, M., 1996. Generalized gradient approximation made simple. Phys. Rev. Lett. 77 (18), 3865.

Piskunov, S., Heifets, E., Jacob, T., Kotomin, E.A., Ellis, D.E., Spohr, E., 2008. Electronic structure and thermodynamic stability of LaMnO 3 and La 1− x Sr x MnO 3 (001) surfaces: Ab initio calculations. Phys. Rev. B—Condens. Matter Mater. Phys. 78 (12), 121406.

Shen, F., Liu, J., Zhang, Z., Dai, J., 2015. On-line analysis and kinetic behavior of arsenic release during coal combustion and pyrolysis. Environ. Sci. Technol. 49 (22), 13716–13723.

Sun, S., Zhang, D., Li, C., Wang, Y., 2015. DFT study on the adsorption and dissociation of H 2 S on CuO (111) surface. RSC Adv. 5 (28), 21806–21811.

Tao, L., Guo, X., Zheng, C., 2013. Density functional study of Hg adsorption mechanisms on α-Fe2O3 with H2S. Proceed. Combust. Instit. 34 (2), 2803–2810.

Wang, V., Xu, N., Liu, J.-C., Tang, G., Geng, W.-T., 2021. VASPKIT: A user-friendly interface facilitating high-throughput computing and analysis using VASP code. Comput. Phys. Commun. 267, 108033.

Wang, Z., Liu, J., Yang, Y., Yu, Y., Yan, X., Zhang, Z., 2020. Experimental and DFT studies of the role of H2S in Hg0 removal from syngas over CuMn2O4 sorbent. Chem. Eng. J. 391, 123616.

Wang, Z., Liu, J., Yang, Y., Yu, Y., Yan, X., Zhang, Z., 2020. Insights into the catalytic behavior of LaMnO3 perovskite for Hg0 oxidation by HCl. J. Hazard. Mater. 383, 121156.

Yan, X., Liu, J., Yang, Y., Wang, Z., Zheng, Y., 2021. A catalytic reaction scheme for NO reduction by CO over Mn-terminated LaMnO3 perovskite: A DFT study. Fuel Process. Technol. 216, 106798.

Yang, Y., Liu, J., Shen, F., Zhao, L., Wang, Z., Long, Y., 2016. Kinetic study of heterogeneous mercury oxidation by HCl on fly ash surface in coal-fired flue gas. Combust. Flame 168, 1–9.

Yang, Y., Liu, J., Zhang, B., Liu, F., 2017. Mechanistic studies of mercury adsorption and oxidation by oxygen over spinel-type MnFe2O4. J. Hazard. Mater. 321, 154–161.

Yi, W., Tang, G., Chen, X., Yang, B., Liu, X., 2020. qvasp: A flexible toolkit for VASP users in materials simulations. Comput. Phys. Commun. 257, 107535.

Zhang, J., Liu, M., Zhang, R., Wang, B., Huang, Z., 2017. Insight into the properties of stoichiometric, reduced and sulfurized CuO surfaces: Structure sensitivity for H2S adsorption and dissociation. Molecul. Cataly. 438, 130–142.

Zhao, H., Tian, X., Ma, J., Su, M., Wang, B., Mei, D., 2020. Development of tailor-made oxygen carriers and reactors for chemical looping processes at Huazhong University of Science & Technology. Int. J. Greenh. Gas Control 93, 102898.

Zheng, C., Zhao, H., 2021. Interaction mechanism among CO, H2S and CuO oxygen carrier in chemical looping combustion: A density functional theory calculation study. Proceed. Combust. Instit. 38 (4), 5281–5288.

Zhu, X., Li, K., Neal, L., Li, F., 2018. Perovskites as geo-inspired oxygen storage materials for chemical looping and three-way catalysis: a perspective. ACS Catal. 8 (9), 8213–8236.